

# A 40-Gb/s PAM-4 Transmitter Based on a Ring-Resonator Optical DAC in 45-nm SOI CMOS

Sajjad Moazeni, *Student Member, IEEE*, Sen Lin, Mark Wade, Luca Alloatti, Rajeev J. Ram, *Fellow, IEEE*, Miloš Popović, *Member, IEEE*, and Vladimir Stojanović, *Senior Member, IEEE*

**Abstract**—The next generations of large-scale data-centers and supercomputers demand optical interconnects to migrate to 400G and beyond. Microring modulators in silicon-photonics VLSI chips are promising devices to meet this demand due to their energy efficiency and compatibility with dense wavelength division multiplexed chip-to-chip optical I/O. Higher order pulse amplitude modulation (PAM) schemes can be exploited to mitigate their fundamental energy-bandwidth tradeoff at the system level for high data rates. In this paper, we propose an optical digital-to-analog converter based on a segmented microring resonator, capable of operating at 20 GS/s with improved linearity over conventional optical multi-level generators that can be used in a variety of applications such as optical arbitrary waveform generators and PAM transmitters. Using this technique, we demonstrate a PAM-4 transmitter that directly converts the digital data into optical levels in a commercially available 45-nm SOI CMOS process. We achieved 40-Gb/s PAM-4 transmission at 42-fJ/b modulator and driver energies, and 685-fJ/b total transmitter energy efficiency with an area bandwidth density of 0.67 Tb/s/mm<sup>2</sup>. The transmitter incorporates a thermal tuning feedback loop to address the thermal and process variations of microrings' resonance wavelength. This scheme is suitable for system-on-chip applications with a large number of I/O links, such as switches and general-purpose and specialized processors in large-scale computing and storage systems.

**Index Terms**—Optical digital-to-analog converter (ODAC), optical interconnects, optical ring resonators, optoelectronics, pulse amplitude modulation (PAM)-4 transmitters, silicon photonics.

## I. INTRODUCTION

SILICON photonics is a promising technology to realize low-cost and energy-efficient optical links for emerging

Manuscript received April 16, 2017; revised July 11, 2017 and August 24, 2017; accepted August 25, 2017. Date of publication October 3, 2017; date of current version November 21, 2017. This paper was approved by Guest Editor Mounir Meghelli. This work was supported in part by DARPA POEM under Award HR0011-11-C-0100, in part by NSF ECCS under Award 1611296, and in part by the Berkeley Wireless Research Center. (*Corresponding author: Sajjad Moazeni*.)

S. Moazeni, S. Lin, and V. Stojanović are with the Department of Electrical Engineering and Computer Science, University of California, Berkeley, CA 94709 USA (e-mail: smoazeni@berkeley.edu).

M. Wade is with Ayar Labs, San Francisco, CA 94107 USA.

L. Alloatti is with the Department of Information Technology and Electrical Engineering, ETH Zurich, 8092 Zurich, Switzerland.

R. J. Ram is with the Department of Electrical Engineering and Computer Science, Massachusetts Institute of Technology, Cambridge, MA 02139 USA.

M. Popović is with the Department of Electrical and Computer Engineering, Boston University, Boston, MA 02215 USA.

Color versions of one or more of the figures in this paper are available online at <http://ieeexplore.ieee.org>.

Digital Object Identifier 10.1109/JSSC.2017.2748620

ing short-reach intra-rack and rack-to-rack interconnects in data-center and high-performance computing applications [1]. This technology also enables high-radix network switches, scalable interconnect fabric for future memory systems, and core-to-core crossbars [2]–[4] once it is integrated with the large-scale electronic system-on-chips. The high performance in all of the abovementioned applications requires tightly integrated electronic-photonic circuits. Various integration strategies have been utilized to meet these demands including hybrid [5], heterogeneous via 3-D stacking [6]–[8], and monolithic [9]–[12] integration. Among these, monolithic integration has the potential for reliable, low-cost, and large-scale integration, while being most promising in terms of energy efficiency and bandwidth density.

Today's silicon photonic links still do not meet the cost and energy requirements of future interconnects due to high integration/packaging costs and the poor energy efficiency of laser sources. Their wall-plug efficiencies are below 10% over the standard temperature range, despite many efforts to heterogeneously integrate uncooled lasers [13], [14]. Hence, scaling the overall link data rate by increasing data rates per wavelength is a favorable direction as long as it also improves the energy efficiency. However, designing energy-efficient optical transceivers at data rates beyond 50-Gb/s is a challenging problem. Bandwidth limitations of optical modulators and directly modulated lasers are leading optical links toward using higher order modulations to increase the spectral efficiency. Pulse amplitude modulation (PAM)-4 has been recently adopted in optical transceivers to double the data rate and accommodate the emerging PAM-4 electrical line rates and modulation formats without the need to introduce the PAM-4 to non-return-to-zero (NRZ) gearshift boxes. For instance, all of the proposed long-reach 400G IEEE standards (400G-DR4, 400G-FR8, and 400G-LR8) are based on this scheme. Multi-level optical modulation can be realized with an electrical digital-to-analog converter (DAC) driving an optical Mach-Zehnder interferometer (MZI) modulator and/or segmenting the phase-shift portions of the MZI and driving them digitally [11]. However, MZIs with high-enough extinction ratio (ER) are inherently millimeter-sized devices, which leads to high energy consumption, high insertion loss (IL), and large footprints. These transmitters have energy efficiencies around 5-pJ/b, which ironically dominates the total link power budget. MZIs with improved phase shifters [15], [16] cannot alleviate this issue as their fabrication in advanced monolithic CMOS

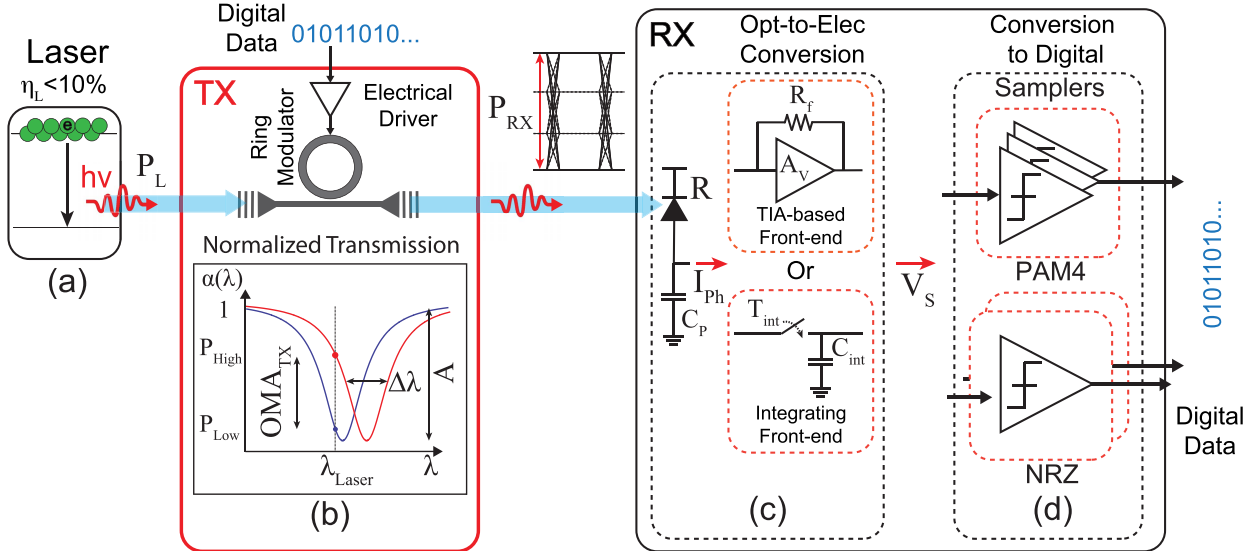


Fig. 1. A ring-resonator-based optical link. (a) Laser source. (b) Transmitter. (c) Receiver's front-end. (d) Receiver's samplers.

processes is problematic, requiring hybrid integration which in turn reduces energy efficiency.

Silicon microring resonators proved to be energy-efficient, compact, and CMOS-compatible devices for high-speed optical transmitters [17]. Moreover, their wavelength selectivity enables dense wavelength division multiplexed (DWDM) links at the micrometer scale and consequently increases aggregate link bandwidth drastically. The thermal and process variation sensitivity issues of microring modulators have been also addressed [18]. However, microring modulators have limited optical bandwidths due to their resonant nature, which constrains the link performance by trading-off the optical modulation amplitude (OMA) with the optical bandwidth [19]. Optical PAM-4 microring modulators have been recently demonstrated [20] in a hybrid platform using an electrical DAC driver.

In this paper, we demonstrate an optical DAC (ODAC) based on a segmented ring resonator in an unmodified (“zero-change”) state-of-the-art 45-nm SOI CMOS monolithic platform [21]. Using this scheme, we propose an O-band optical PAM-4 transmitter, which eliminates the electrical DAC and its non-linearity, power consumption, and area overhead. Measurements show two orders of magnitude improvement in the energy efficiency compared with the MZI-based PAM-4 transmitters. This high-speed resonant ODAC also enables a multitude of optical pulse shaping applications such as optical arbitrary waveform generators (AWG) and RF photonics [22]–[24].

This paper is organized as follows. Section II describes the benefits of using PAM-4 over conventional NRZ modulation in ring-resonator-based optical links. Section III introduces the 45-nm SOI CMOS photonic platform. The idea of a segmented ring-resonator-based ODAC is presented in Section IV. Sections V and VI elaborate on the transmitter’s architecture and building blocks. Experimental results are discussed in Section VII and compared with prior works in Section VIII. Section IX concludes this paper.

## II. CHOOSING THE RIGHT MODULATION

In this section, we present an overview of the ring-resonator-based optical link elements and compare the energy efficiency of PAM-4 and NRZ modulation schemes for these links.

### A. Ring-Resonator-Based Optical Links

Fig. 1 shows an optical link with a ring-resonator-based transmitter. For simplicity, we focus on a single wavelength link, while the following discussion can be extended to DWDM optical links as well. Light from a single wavelength,  $\lambda_{\text{Laser}}$ , laser source [Fig. 1(a)] with wall-plug efficiency of  $\eta_L$  and output optical power of  $P_L$  is coupled into the transmitter. On the transmit side [Fig. 1(b)], a microring resonator imprints the digital data stream in the input light. Microring resonators are waveguide loops coupled into a bus waveguide, which trap the input light’s wavelength  $\lambda$  inside the loop (cavity) whenever the round trip optical length is an integer multiple of  $\lambda$ . Thus, the microring resonator acts as an optical filter with a resonance wavelength of

$$\lambda_0 = (n_{\text{eff}} \cdot L)/m \quad (1)$$

where  $n_{\text{eff}}$  is the effective refractive index,  $L$  represents the ring’s circumference, and  $m$  is the integer number associated with this resonance. Normalized thru-port transmission,  $\alpha(\lambda)$ , of a ring resonator around this resonance wavelength can fit to a Lorentzian characteristic [10], [18] as follows:

$$\alpha(\lambda) = 1 - \frac{A}{1 + 4 \left( \frac{\lambda - \lambda_0}{\Delta\lambda} \right)^2} \quad (2)$$

where  $\Delta\lambda$  is the linewidth around the  $\lambda_0$  resonance. The constant  $A$  is indicative of device intrinsic extinction.  $A = 1$  when the device is perfectly critically coupled [12] such that  $\alpha(\lambda_0) = 0$ . The ring’s Q-factor is equivalent to  $\lambda_0/\Delta\lambda$ , which depends on the round trip optical loss and also the coupling strength to the bus waveguide. The Lorentzian transmission and relevant parameters are detailed in Fig. 1(b).

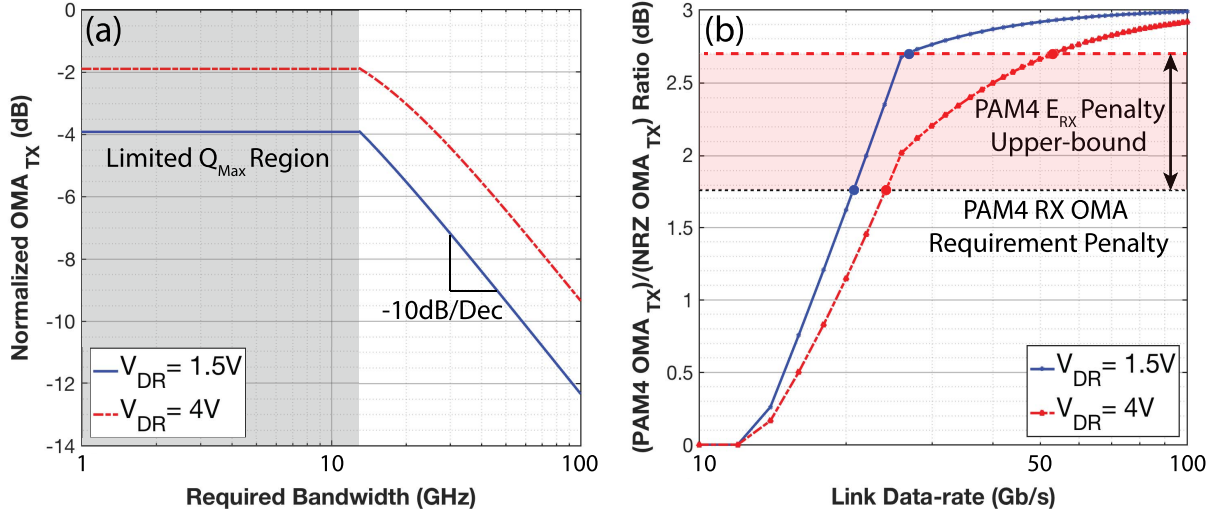


Fig. 2. (a) Normalized achievable OMA<sub>Tx</sub> of a ring modulator versus the required bandwidth. (b) Ratio of PAM-4 OMA<sub>Tx</sub> over NRZ. The energy efficiency improvement at any data rate is determined by the difference of this curve and the PAM-4 receivers' energy penalty (black/red dashed lines).

Active microrings can be built using *p-n* or *p-i-n* junctions capable of shifting the resonance wavelength via the free carrier plasma dispersion effect [25], [26]. The amount of resonance shift is a function of the applied voltage, doping profiles, and junctions' geometry. This resonance shift can be utilized for the amplitude modulation of a carrier wavelength. Fig. 1(b) illustrates an example of ON-OFF keying modulation, where the transmitted light intensity is digitized in  $P_{\text{High}}$  and  $P_{\text{Low}}$  levels. The separation of the highest and lowest normalized optical powers ( $P_{\text{High}} - P_{\text{Low}}$ ) in any PAM modulation can be defined as the transmitter OMA (OMA<sub>Tx</sub>), which depends on the Q-factor and the amount of resonance shift. Since, the resonance shift is governed mainly by the electrical and optical capabilities of the technology, OMA<sub>Tx</sub> is dictated by the Q-factor. However, Q-factor should be proportionally decreased as data rate increases to provide enough optical bandwidth for the inter-symbol interference (ISI)-free communication [19]. Fig. 2(a) presents the achievable OMA<sub>Tx</sub> for different required bandwidths. In this model, the ring is always critically coupled with  $A = 0.9$  and resonance wavelength shift of 20 pm/V of reverse bias voltage. Applied voltage is determined by the driver's voltage swing ( $V_{\text{DR}}$ ), set to 1.5 V (for CMOS inverter-based drivers used in this paper) or 4 V, that can be achieved by differential thick-oxide or cascode drivers [27]. A further increase in  $V_{\text{DR}}$  is not helpful due to the limited depletion region width of the junctions in addition to energy consumption and bandwidth limitation overheads of the higher swing drivers. The OMA<sub>Tx</sub> curve is flat at low bandwidths since the Q-factor cannot be higher than  $Q_{\text{Max}}$ , determined by the carrier absorption and intrinsic optical loss mechanisms inside the cavity ( $Q_{\text{Max}} = 18$  k assumed here [28]).

OMA at the receiver is denoted by  $P_{\text{RX}}$ , which can be calculated by knowing the total optical path loss that includes the three couplers and waveguide/fiber losses,  $\Gamma_L$ , from ( $P_{\text{RX}} = P_L \cdot \Gamma_L \cdot \text{OMA}_{\text{Tx}}$ ). In the receiver front-end [Fig. 1(c)], optical power is converted into the photocurrent ( $I_{\text{Ph}} = R \cdot P_{\text{RX}}$ ), where  $R$  represents the responsivity of the

photodiode (PD) with a parasitic capacitance of  $C_P$ . This current undergoes amplification either via a trans-impedance amplifier (TIA) [29] or an integrator [30]. The conversion gain, 3-dB bandwidth ( $BW$ ), and the input referred current noise ( $\sigma_n$ ) can be estimated for the TIA-based front-ends as follows:

$$\begin{aligned} \text{Gain} &= \frac{V_S}{I_{\text{Ph}}} \approx R_f, \quad BW = \frac{1 + A_V}{2\pi C_p R_f} \\ \sigma_n &= \frac{1}{\text{Gain}} \sqrt{\frac{4kT(1 + A_V)}{2\pi C_p} + \sigma_{v,\text{Amp}}^2 + \sigma_{v,\text{Dig}}^2} \end{aligned} \quad (3)$$

where  $R_f$  is the feedback resistance,  $A_V$  is the amplifier's open loop voltage gain,  $k$  denotes the Boltzmann constant, and  $T$  is the temperature. Here we assume the input pole with ( $C_{\text{in}} \approx C_p$ ) is dominant and  $\sigma_{v,\text{Amp}}$  and  $\sigma_{v,\text{Dig}}$  denote the voltage noise of the amplifier and samplers, respectively. For the integrating front-ends, gain depends on the integration period, normally a fraction ( $k_{\text{int}} < 1$ ) of the symbol time ( $T_{\text{Sym}}$ )

$$\begin{aligned} \text{Gain} &= \frac{k_{\text{int}} T_{\text{Sym}}}{C_{\text{int}} + C_p}, \quad BW = \frac{1}{2\pi(C_p \parallel C_{\text{int}}) R_{\text{ON}}} \\ \sigma_n &= \frac{1}{\text{Gain}} \sqrt{\frac{kT}{(C_p \parallel C_{\text{int}})} + \sigma_{v,\text{Dig}}^2} \end{aligned} \quad (4)$$

where  $R_{\text{ON}}$  is the ON resistance of the integration switch and  $C_{\text{int}}$  is the integration capacitance. Finally, the resultant voltage,  $V_S$ , should be converted back into the digital domain via a set of samplers [Fig. 1(d)]. Samplers require a minimum voltage swing,  $V_{S,\text{Min}}$ , in order to resolve the input analog voltage into the digital symbols. The receiver requires a minimum OMA level,  $P_{\text{RX},\text{Min}}$ , at each data rate in order to satisfy the sampler's sensitivity and signal-to-noise ratio requirements and achieve the target bit error rate consequently.  $P_{\text{RX},\text{Min}}$  also depends on timing related jitter, which is ignored in this first-order analysis under ISI-free conditions.

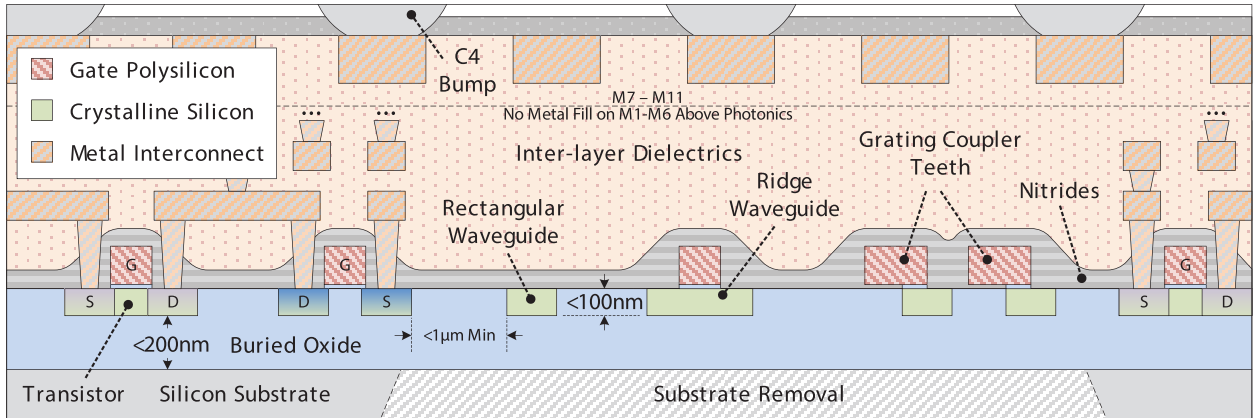


Fig. 3. Cross section of the “zero-change” 45-nm SOI platform [18] (not drawn to scale).

### B. Energy Efficiency Comparison of PAM-4 and NRZ

Total energy efficiency (per bit) can be expressed as  $E_{\text{tot}} = E_L + E_{\text{TX}} + E_{\text{RX}}$ , where the terms correspond to the energy efficiency of the laser, the transmitter, and the receiver, respectively. In monolithic ring-resonator-based transmitters,  $E_{\text{TX}}$  is strictly dominated by the serializer and clocking blocks since the required driver size to drive a microring’s capacitance is relatively small. Therefore, we assume  $E_{\text{TX}}$  is a fixed technology-dependent parameter, which can be optimized independently. Considering high optical losses and inefficient laser sources in today’s optical links,  $E_L$  dominates the total link energy budget. Furthermore, improving  $E_L$  leads to laser integration and packaging cost reduction in addition to improving the form factor. Laser energy per bit at the DR data rate can be obtained from the following:

$$E_L = \frac{P_{\text{RX},\text{Min}}}{\eta_L \cdot \Gamma_L \cdot \text{OMA}_{\text{TX}} \cdot \text{DR}}. \quad (5)$$

According to Fig. 2(a), PAM-4 transmitters provide a larger  $\text{OMA}_{\text{TX}}$  compared with the NRZ at the same data rate since they require half the bandwidth. However, PAM-4 receivers require larger  $P_{\text{RX},\text{Min}}$  due to the  $3\times$  reduction in symbol level separation. In order to estimate the penalty in  $P_{\text{RX},\text{Min}}$ , we consider a case where PAM-4 and NRZ receivers both have the same sampler’s sensitivity for a fixed data rate. This is illustrated in Fig. 1(d), where three samplers in PAM-4 and two for NRZ case operate at the same sampling rate. Equations 3 and 4 imply that PAM-4 receivers have two times larger Gain and therefore half the noise level  $\sigma_n$  (assuming constant  $\sigma_{v,\text{Amp}}$  and  $\sigma_{v,\text{Dig}}$ ). This can be realized by doubling  $R_f$  in the TIA-based or equivalently doubling the  $T_{\text{Sym}}$  in these equations. Combining this with  $3\times$  reduction in nearest symbol level distance, the  $P_{\text{RX},\text{Min}}$  is  $1.5\times$  larger for a PAM-4 receiver to satisfy the sampler’s sensitivity requirement. This penalty is smaller in practice taking the amplifiers’ bandwidth limitations [31] and the adjustment of integration capacitances into account.

Hence, if PAM-4  $\text{OMA}_{\text{TX}}$  is larger than the NRZ by more than ( $1.5\times \approx 1.76\text{-dB}$ ) at any data rate, the optical energy efficiency of the link will be improved by exploiting PAM-4 modulation. Fig. 2(b) shows the ratio of the  $\text{OMA}_{\text{TX}}$  for PAM-4 and NRZ along with the  $1.76\text{-dB}$  penalty of the PAM-4

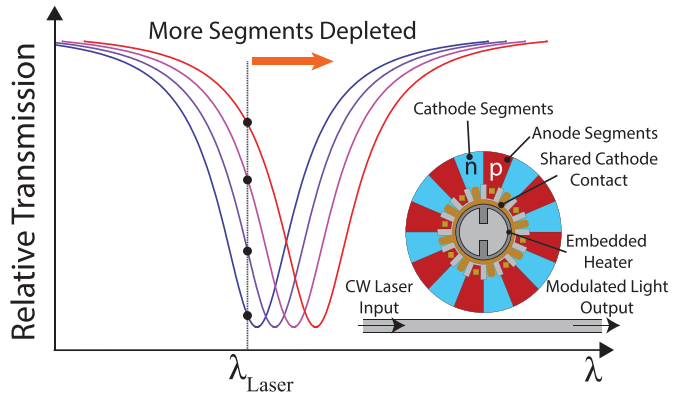


Fig. 4. Segmented ring-resonator ODAC concept.

receivers’ OMA requirement (black dashed line) versus data rate for two different  $V_{\text{DR}}$  values. For data rates above the crossover points, PAM-4 links require less optical energy. As the laser energy improves, we may reach a point where receiver energy becomes comparable with the optical energy ( $E_{\text{RX}} \approx E_L$ ) suggesting that PAM-4  $E_{\text{RX}}$  overhead due to the larger number of samplers should be taken into account as well. The upper bound for this dynamic energy overhead is 50%, as the receivers are operating at the same data rate and clock frequency and the number of samplers’ ratio is 3:2 [Fig. 1(d)]. Dynamic energy is about half of the energy consumption of the optical receivers [29], [30], and thus PAM-4  $E_{\text{RX}}$  overhead is at most 25% ( $\approx 1\text{-dB}$ ) (red dashed line). Notice here we ignored all the static energy savings of PAM-4 receivers due to the relaxed bandwidth requirement. In addition, energy efficiency of the NRZ receivers degrades more rapidly since samplers’ noise starts dominating due to the more required time interleaving and lower available Gain at high data rates [32], [33]. The red dashed line in Fig. 2(b) shows the new PAM-4 receivers’ energy overhead by adding the  $E_{\text{RX}}$  overhead upper bound to the OMA requirement penalty (black dashed line). In practice, PAM-4 starts improving the total energy efficiency for data rates higher than a point in between the crossover of the OMA improvement curve with two penalty lines, depending on the actual optimized PAM-4 receivers’ energy overhead. A similar analysis can be applied to other silicon photonics technologies and higher order PAM modulations such as PAM-8/16 as well.

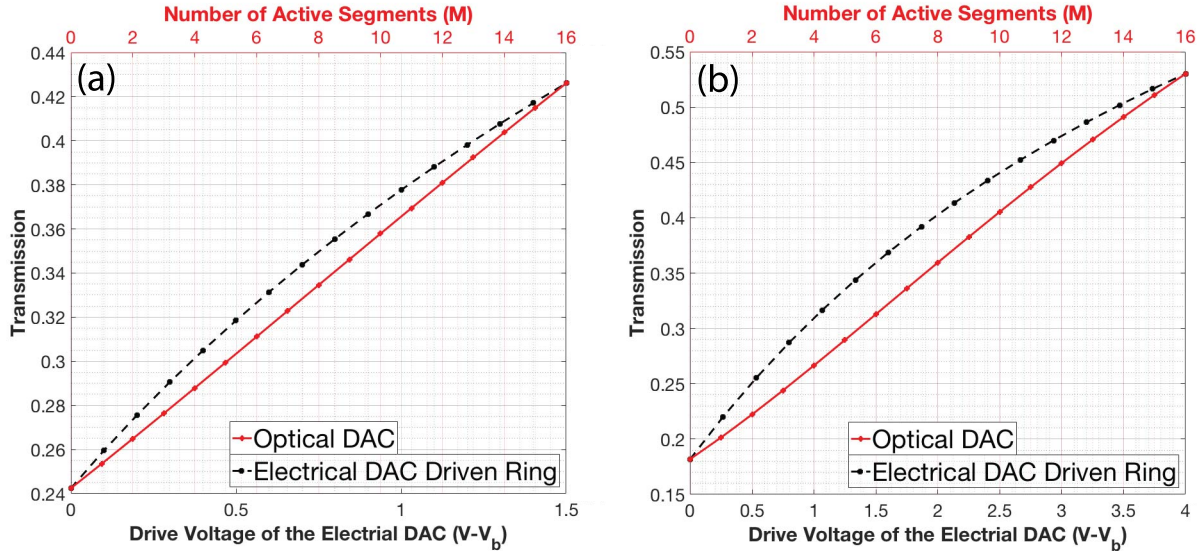


Fig. 5. Linearity comparison of the proposed ODAC versus an ideal electrical DAC driven microring modulator for driver's voltage swings of (a) 1.5 and (b) 4 V.

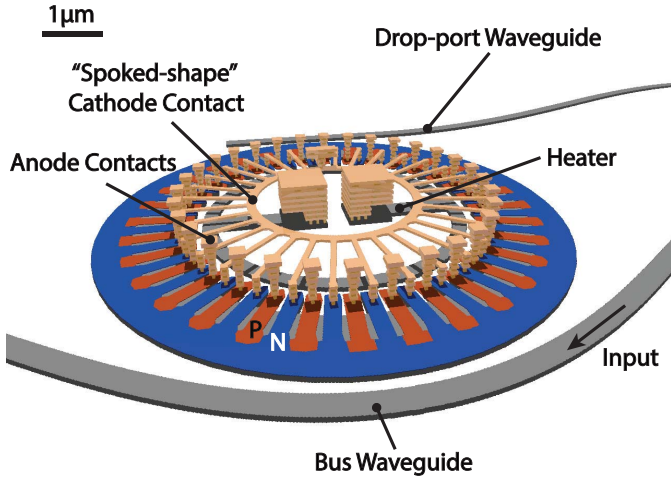


Fig. 6. 3-D layout of a segmented ring-resonator-based ODAC in “zero-change” 45-nm SOI platform.

### III. “ZERO-CHANGE” 45-nm SOI PLATFORM

We implement our proposed ODAC and PAM-4 transmitter designs using an unmodified (“zero-change”) commercial 45-nm CMOS SOI process [34]. Recently, we have demonstrated a photonic link using this technology, where millions of transistors and hundreds of photonic devices have been fabricated in the same chip to improve processor-memory link bandwidth [9], [18]. All photonic devices are designed to conform to the existing (purely electrical) foundry design flow [21], without any modifications to the native process (Fig. 3). Key enabler of optical devices is the sub-100-nm-thick high-index crystalline silicon (c-Si) layer, normally used as the body of transistors. Since the buried oxide layer is not thick enough to optically isolate the c-Si waveguide core from the silicon substrate, we have to remove silicon substrate to reduce the waveguide optical loss. Substrate removal is done in a single post-processing step on the flip-chip die-

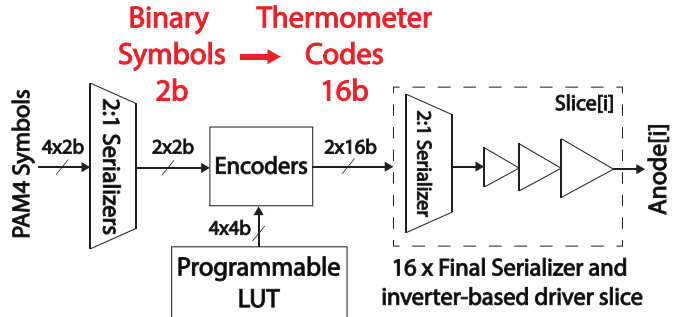


Fig. 7. Block diagram of the transmitter’s data path.

attached chips [21]. The flip-chip underfill keeps the released die mechanically stable and dissipates the heat even under thermal stress tests. Transistors are also unaffected, and all existing foundry IP, timing libraries, and simulation models remain valid [9], [21]. Waveguide loss of approximately 3 dB/cm is achieved after this step. In addition, the flip-chip packaging is favorable for high-performance electronics due to better power delivery, pin counts, and signal integrity of the I/O pins. Light is coupled to the chip via vertical grating couplers. Couplers have been also fabricated by patterning c-Si and polysilicon layers. Polysilicon layer helps to break vertical symmetry and achieve sub-2-dB loss (including the taper) over the 78-nm 1-dB bandwidth around 1320-nm wavelength [35], [36].

Active devices including microring modulators and PDs are demonstrated using existing source/drain and well implant doping levels. Microring modulators have been designed by placing interleaved *p* and *n* junctions along the ring cavity. These 5-μm radius microrings achieved loaded Q-factors of better than 10 k with high thermal tuning efficiencies [ $3.8 \mu\text{W}/\text{GHz}$  with the tuning range of 524-GHz ( $>50\text{-K}$  temperature)] [18], [28]. Resonated SiGe detectors on this platform showed a responsivity of 0.55 A/W [37]. Polysilicon-based resonant detectors have also been

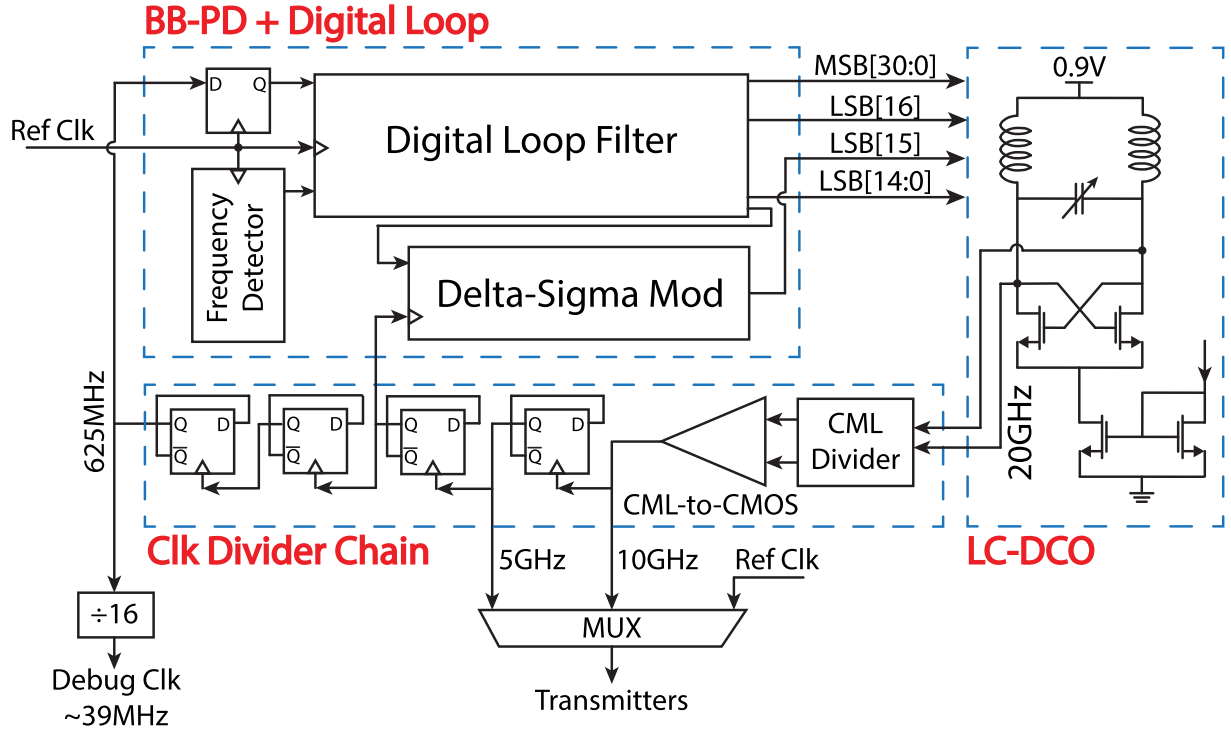


Fig. 8. 20-GHz DPLL's block diagram.

demonstrated covering optical telecommunication bands from O-band to L-band [38].

#### IV. RING-RESONATOR-BASED OPTICAL DAC

In this section, we present the ODAC idea based on a segmented ring-resonator design. First, we characterize the ODAC's transmission and linearity and later describe the implementation details of this device in our "zero-change" platform.

##### A. Optical DAC

Microring resonator-based ODAC can be realized by segmenting the *p-n* junction phase shifter along the ring and driving each of the segments separately. In doing so, the density of carriers in the cavity can be controlled by depleting a certain number of segments, consequently producing a corresponding resonance shift and an optical thru-port intensity change (Fig. 4). For the interleaved junctions, phase shifter is already segmented and we only need to drive each junction segment independently. In order to compare linearity of this approach with the conventional electrical DAC driven microring modulator, we will derive the thru-port transmission as a function of the number of depleted junctions and the applied voltage. First, we derive the resonance wavelength shift ( $\lambda_{\text{Shift}}$ ) and later substitute it in the Lorentzian characteristic of the ring resonator (2).  $\lambda_{\text{Shift}}$  caused by a perturbation in the effective refractive index ( $\Delta n_{\text{eff}}$ ) can be directly obtained from (1) as

$$\lambda_{\text{Shift}} = (L/m) \cdot \Delta n_{\text{eff}}, \quad \Delta n_{\text{eff}} = \gamma \cdot (k_e \cdot \Delta N_e + k_h \cdot \Delta N_h) \quad (6)$$

where  $\Delta n_{\text{eff}}$  is a linear function of the electron/hole density change ( $\Delta N_e / \Delta N_h$ ) [25],  $\gamma$  expresses the effective

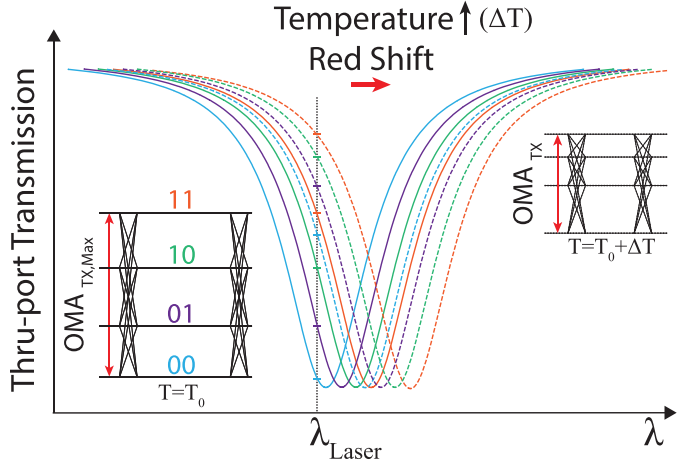


Fig. 9. Thermal sensitivity of the resonance wavelength and its effects on a PAM-4 transmit eye. PAM-4 levels are uncoded while any coding can be applied through the LUT.

interaction of optical mode with depletion regions, and  $k_e / k_h$  are material- and optical band-dependent coefficients. Since carrier injection modulators are slow due to the long carrier life time in the *p-n* junctions along the cavity [39], only depletion mode (reverse bias) operation is considered. Assuming an abrupt *p-n* junction model, N side depletion region's width for a single junction can be derived in terms of the N and P side doping concentrations ( $N_D$ ) and ( $N_A$ ), junction's built-in voltage ( $V_b$ ), dielectric permittivity of the silicon ( $\epsilon_{\text{Si}}$ ), and elementary charge ( $q$ ) as follows:

$$x_e(V) = \frac{1}{N_D} \sqrt{\frac{2\epsilon_{\text{Si}}(V + V_b)}{q}} \frac{N_A N_D}{N_A + N_D} \quad (7)$$

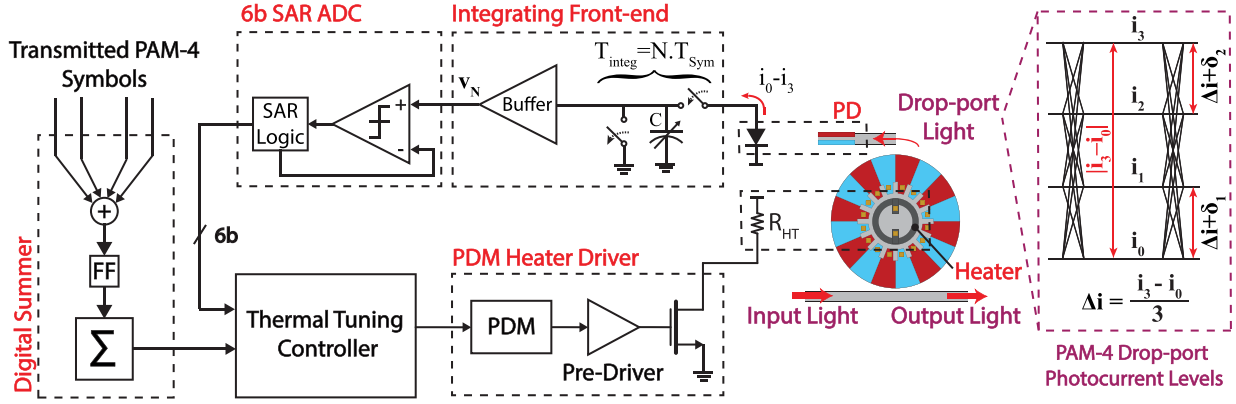


Fig. 10. PAM-4 transmitter's thermal tuning feedback loop block diagram.

where  $V$  is the applied reverse bias voltage of the segments. By summing over all the depleted segments,  $M$ , total change in electron/hole density per  $\text{cm}^3$  can be obtained from

$$\Delta N_e = \frac{M \times N_D \Delta x_e}{L} = \frac{M \times N_D}{L} \frac{x_e(0)}{\sqrt{V_b}} (\sqrt{V + V_b} - \sqrt{V_b}). \quad (8)$$

Since  $N_D x_e = N_A x_h$  holds, we suppose  $\Delta N_h = \Delta N_e$ . Finally, we can derive  $\lambda_{\text{Shift}}$  as a function of  $M$  and  $V$  from (6) and (8), and rewrite (2) in terms of the  $\lambda_{\text{Shift}}(M, V)$  as

$$\lambda_{\text{Shift}}(M, V) = M(\sqrt{V + V_b} - \sqrt{V_b}) \times \left[ \gamma \frac{k_e + k_h}{m} \sqrt{\frac{2\epsilon_{\text{Si}}}{q}} \frac{N_A N_D}{N_A + N_D} \right] \quad (9)$$

$$\alpha_{M,V}(\lambda) = 1 - \frac{A}{1 + 4 \left( \frac{\lambda - \lambda_0 - \lambda_{\text{Shift}}(M,V)}{\Delta\lambda} \right)^2}. \quad (10)$$

Fig. 5 depicts the normalized transmission function,  $\alpha_{M,V}(\lambda)$ , for an ODAC and an ideal electrical DAC driven ring modulator.  $\lambda$  is set to the wavelength that maximizes the OMA<sub>TX</sub> for a microring with  $\lambda_0 = 1280\text{-nm}$ ,  $Q = 7.5\text{ k}$ ,  $A = 0.9$ ,  $V_b = 0.5\text{ V}$ , 16 junction segments, and 20-pm resonance shift at 1 V applied voltage. Two different driving voltage capabilities (1.5 and 4 V) are also considered to study the effect of the maximum resonance shift on the linearity of both methods. ODAC shows a slight improvement for the smaller range resonance shifts [Fig. 5(a)] while showing higher improvement for larger shifts [Fig. 5(b)]. Notice here we assumed that the electrical DAC is ideal, while designing a linear electrical DAC operating at +20 GS/s is not trivial and requires extra area and energy overhead. Our analysis also showed that the effects of the optical loss variations inside the cavity due to the different depleted carriers' density on the linearity of the ODAC are negligible in a PAM-4 transmitter design. The direct digital drive of the ODAC design also lends itself to efficient pre-emphasis equalization, which can help improve the bandwidth limitation of the ring resonators. The pre-distortion of the ODAC non-linearity is critical in some applications such as high-resolution optical AWGs.

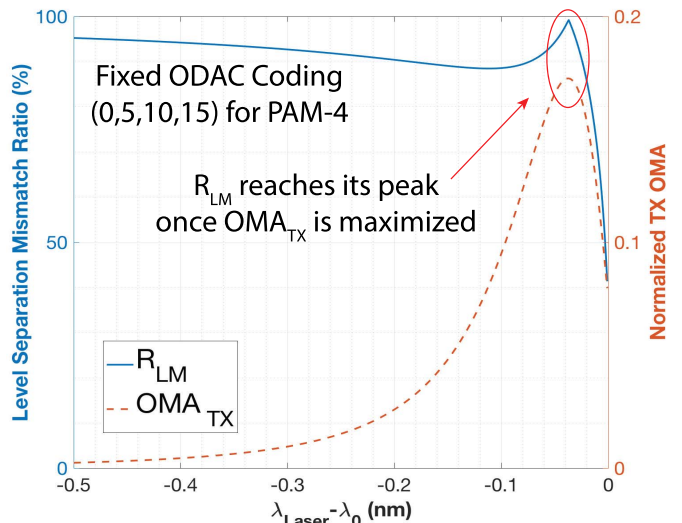


Fig. 11. OMA<sub>TX</sub> and PAM-4 level-mismatch ratio versus the relative distance of the ring's resonance and laser's wavelength.

#### B. Segmented Ring-Resonator ODAC in “Zero-Change” 45-nm SOI Platform

ODAC is built using interleaved lateral  $p$ - $n$  “T-junctions” with the cavity diameter of 10  $\mu\text{m}$  in “zero-change” 45-nm SOI platform [40] (Fig. 6). Although more segments increase the resolution of the ODAC, the number of segments is limited to the minimum allowed doping region's width set by the technology design rules. In the current design, we choose to place 64 segments (32 anodes and 32 cathodes) along the ring, while 128 is the upper limit with current junction shapes. All the cathode segments are connected together via a spoked-ring shape metal contact in the center of the ring, while each anode segment has its own contact pin. The spoked-shape contact prevents extra optical loss due to the proximity of the electrical metal and contacts to the inner radius of the ring waveguide [28]. A resistive c-Si-based heater and a weakly coupled drop port with a straight PD are also added to this structure for closed-loop thermal tuning of the ring [18].

#### V. OPTICAL PAM-4 TRANSMITTER BLOCKS

ODAC-based PAM-4 transmitter electronics consist of a fully digital data path, a digital phase-locked loop (DPLL),

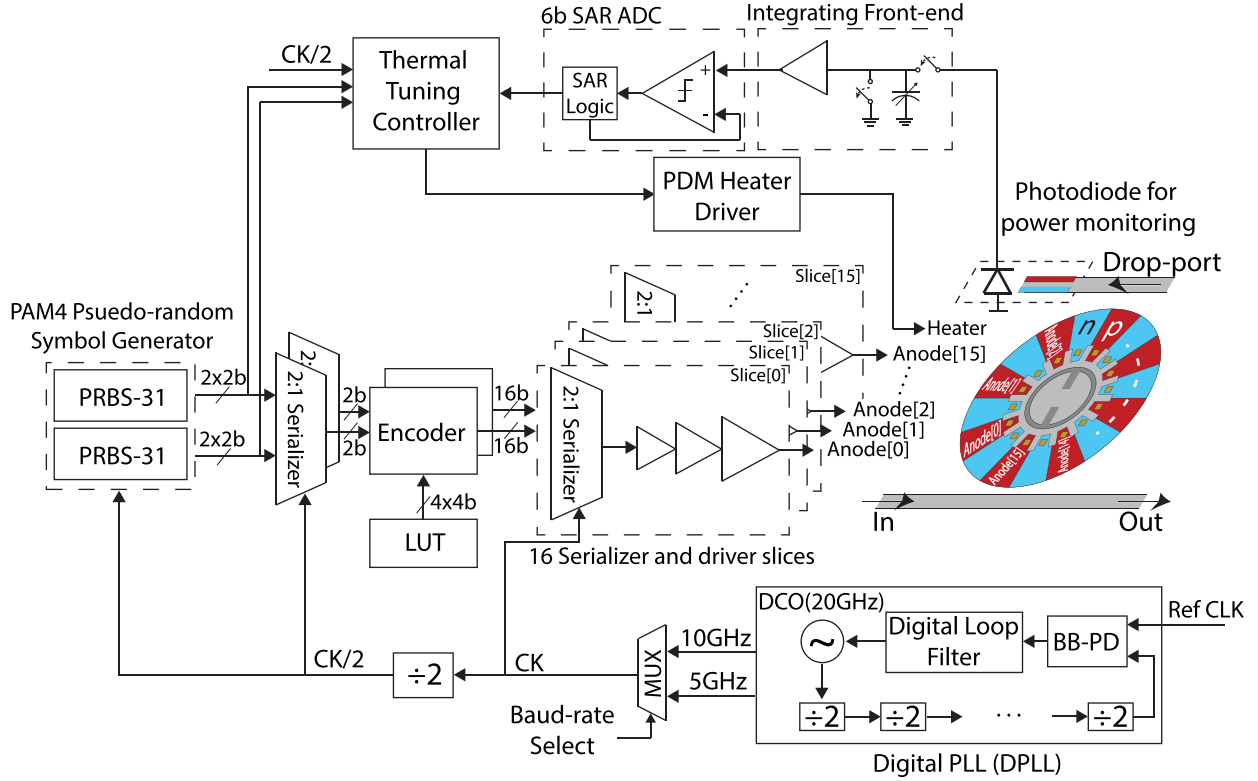


Fig. 12. PAM-4 transmitter's full block diagram.

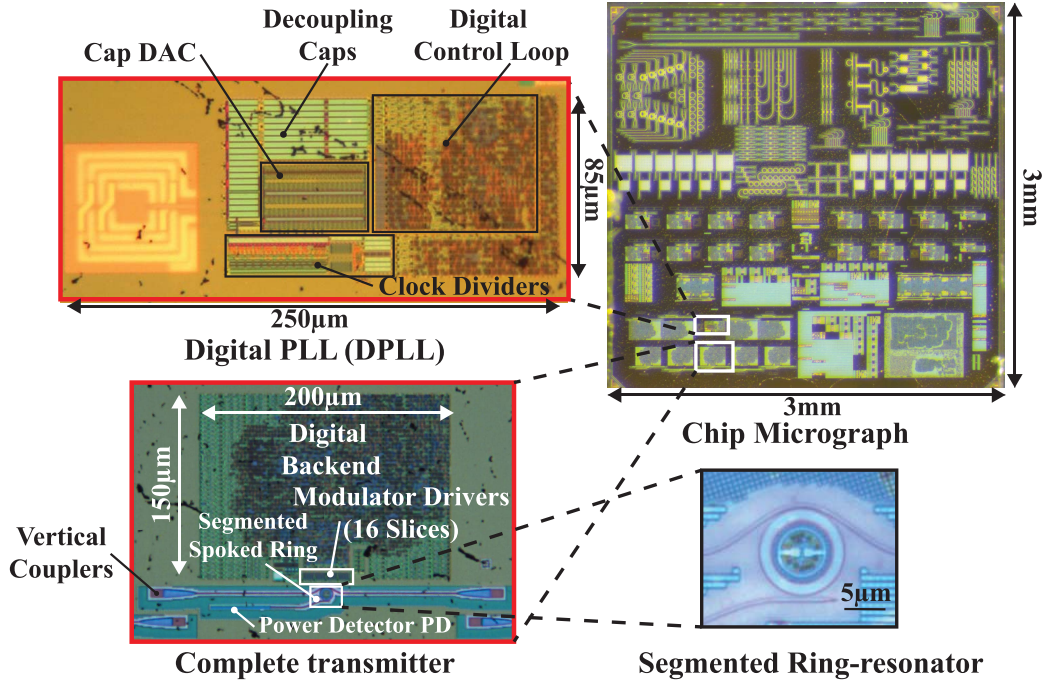


Fig. 13. Micrographs of the test chip, DPLL, full transmitter, and an ODAC.

and a thermal tuning feedback loop. This section explains the design details of each of these blocks.

#### A. Transmitter Data Path

PAM-4 symbols are generated from two separate PRBS-31 modules in the digital backend. While ODAC design has

32 anode junctions, here we drive each two anodes together. The segments are activated in a thermometer manner to achieve better linearity, electrical bandwidth, and energy efficiency, by minimizing the wire-to-wire capacitance parasitics of the segment control wires. This segment partitioning with thermometer coding leads to a 4-bit binary ODAC.

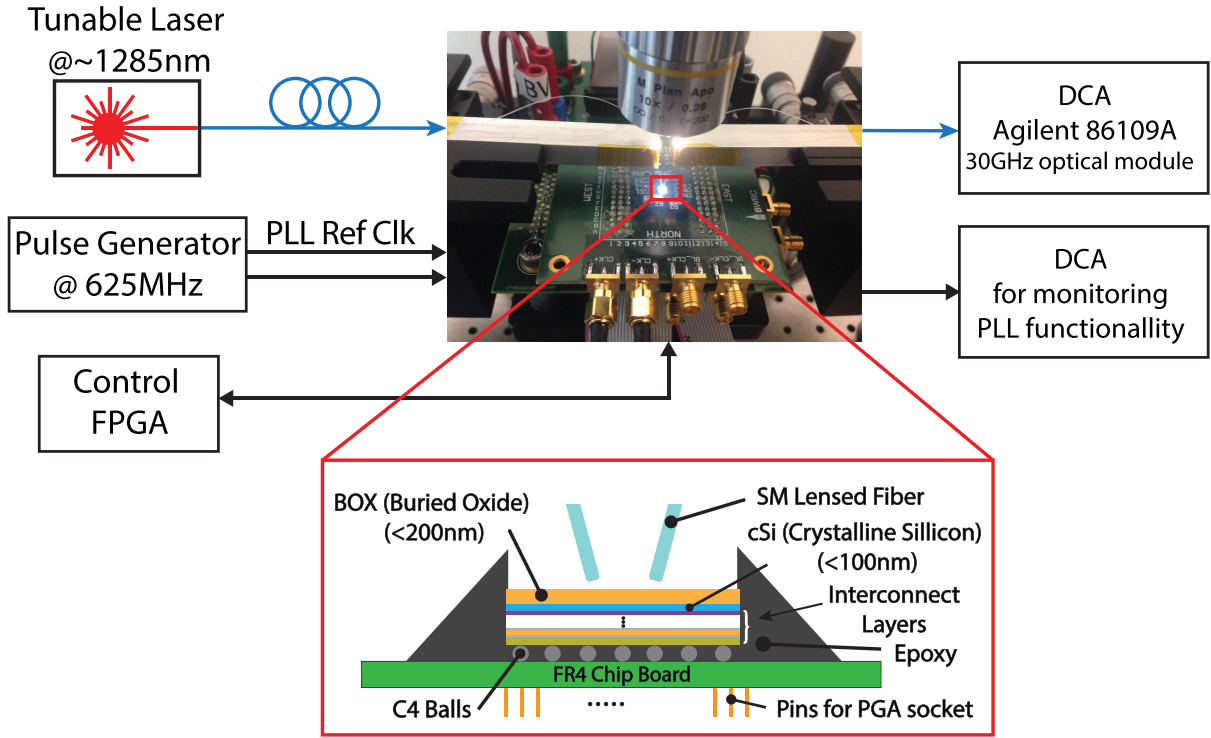


Fig. 14. Test setup and packaging scheme of the test chip.

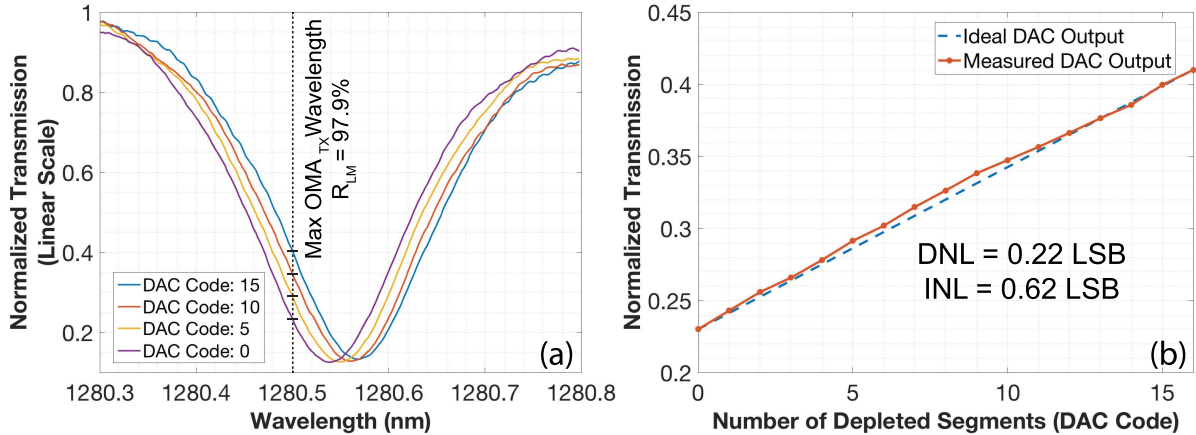


Fig. 15. (a) ODAC static measurement at low optical input power to avoid thermal drifts. Note that the resonance is shifted down to 1280 nm as cavity's optical power and consequently temperature is lower than the eye diagram measurement. (b) Normalized optical output for each DAC code compared with an ideal linear DAC (Code 1's output is derived from Codes 0 and 2 transmissions since it is skipped in transmitter's 16-b thermometer coding).

The mapping is done by grouping the first two segments together so that 16 states of the driver can be matched to the modulator conditions from all to none *p*-*n* junctions depleted. Although PAM-4 symbols consist of 2 bits, the extra 2 bits of the ODAC provide flexibility for linearization of the Lorentzian behavior discussed in Section IV-A. Fig. 7 shows the transmitter data-path's block diagram. MUX-based encoders convert the 2-b PAM-4 symbols to 16-b thermometer codes mapped by a programmable look-up table (LUT). LUT size is only  $4 \times 4\text{-b} = 16\text{-b}$  and it is implemented by scan-flop cells.

#### B. Digital PLL

Transmitter's target symbol rate was 20 GS/s, requiring a 10-GHz clock source as it operates in the double data

rate fashion. Clocking blocks are illustrated in Fig. 8. The DPLL generates a differential 20-GHz clock and divided clocks (10 and 5 GHz) from the PLL clock divider chain can be selected as the transmitter's reference clock. DPLL is composed of an LC-DCO, bang-band phase detector, and a fully digital loop filter [41]. Since the substrate will be removed, we adjusted the inductor design to achieve the target clock frequency. Measured tuning range is 16–22 GHz after the substrate removal as expected from the simulation.

#### C. Thermal Tuning

Despite multiple advantages of microring modulators, there are limited microring-based commercial optical transceivers due to the thermal and process variations of microrings' resonance wavelength [42], [43]. Thermo-optical resonance shift

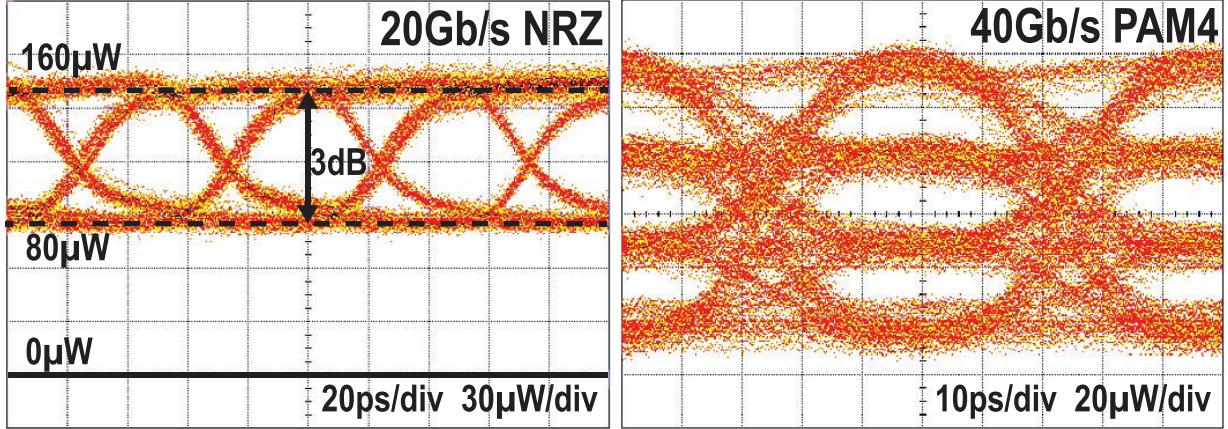


Fig. 16. Measured transmit eye diagrams. The highest and lowest optical levels are the same since the operating point remains the same.

effects are estimated to be as large as  $-10 \text{ GHz/K}$  [43]. Fig. 9 depicts this effect, where solid and dashed lines represent corresponding ring positions to each PAM-4 symbol at temperatures  $T_0$  and  $T_0 + \Delta T$ , respectively. Resonance wavelength is chosen on the right side of the laser wavelength where it is thermally stable [18] such that OMA<sub>TX</sub> is maximized at temperature  $T_0$ . Resonance shift due to increase in the temperature causes unbalanced PAM-4 levels in addition to the degradation of the OMA<sub>TX</sub>. Recently, we have demonstrated a thermal tuner capable of optimizing and locking the ring position in NRZ transceivers regardless of the data encoding [18]. In this paper, we adopt the same scheme and show this approach can be extended for higher order PAM transmitters. Block diagram of the proposed thermal tuner for PAM-4 is shown in Fig. 10. A weakly coupled drop port to the ring senses a small fraction ( $\approx 1\%$ ) of the optical power inside this cavity. Next, the optical power is converted to the equivalent photocurrents (denoted by  $i_{0-3}$ ). The current will be integrated on a capacitor of size  $C$  in an interval of  $N$  symbols. Resultant voltage is digitized via a 6-b analog-to-digital converter and fed into the controller as the sensing input of this feedback loop. Assuming that  $N_n$  denotes the number of “ $n$ ”-level symbols, transmitted during the integration period, the output voltage of the integrator is

$$v_N = \frac{T_{\text{Sym}}}{C} \left( \sum_{n=0}^3 N_n \cdot i_n \right). \quad (11)$$

We can reformulate this by rewriting the intermediate levels in terms of the lowest and highest optical levels ( $i_0$  and  $i_3$ ), assuming the level mismatch around the optimum point is negligible ( $\delta_1, \delta_2 \ll \Delta i$ ) as

$$v_N = \frac{T_{\text{Sym}}}{3C} ((3N_3 + 2N_2 + N_1) \cdot i_3 + (N_2 + 2N_1 + 3N_0) \cdot i_0). \quad (12)$$

The coefficients of  $i_3$  and  $i_0$  are the binary summation over all the transmitted symbols and inverted symbols, respectively. Thus, PAM-4 level extraction equations can be mapped to the equivalent NRZ mode by just modifying the coefficients and the rest of the procedure is similar to the NRZ case [18].

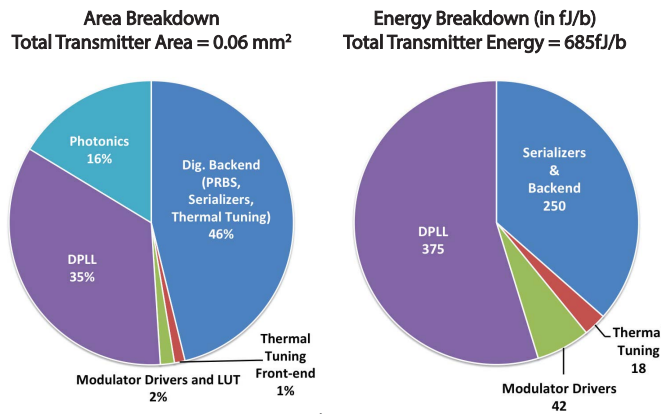


Fig. 17. Transmitter's energy and area breakdown at 40-Gb/s PAM-4.

In a nutshell, the controller can solve (12) for  $i_0$  and  $i_3$  by integrating over two consecutive windows. The tuning procedure starts with sweeping the wavelength resonance by sweeping down the heater strength via pulse density modulation (PDM). Afterward, heater PDM value is set to the optimum value where the maximum of  $(i_3 - i_0)$  occurred. After the optimization phase, controller keeps locking the ring to this position by tracking either “0”-level or “3”-level symbols. Fig. 11 shows the PAM-4 level separation mismatch ratio,  $R_{\text{LM}}$ , and OMA<sub>TX</sub> as a function of the spacing between the microring resonance and laser wavelength.  $R_{\text{LM}}$  is defined as the ratio of the minimum PAM-4 eye height to 1/3 of the OMA<sub>TX</sub>. This simulation validates the  $(\delta_1, \delta_2 \ll \Delta i)$  assumption during the optimization and locking procedures.

## VI. COMPLETE TRANSMITTER DESIGN

The complete ODAC-based PAM-4 transmitter integrates all the sub-blocks described in the previous section (Fig. 12). The transmitter can operate in both NRZ and PAM-4 modes with selectable baud rate of 10 or 20 GS/s. Transmitter is running on the nominal supply of 0.9 V except for the drivers which use 1.55 V. We have not used thick-oxide devices for the driver, using them can reduce the reliability risks and

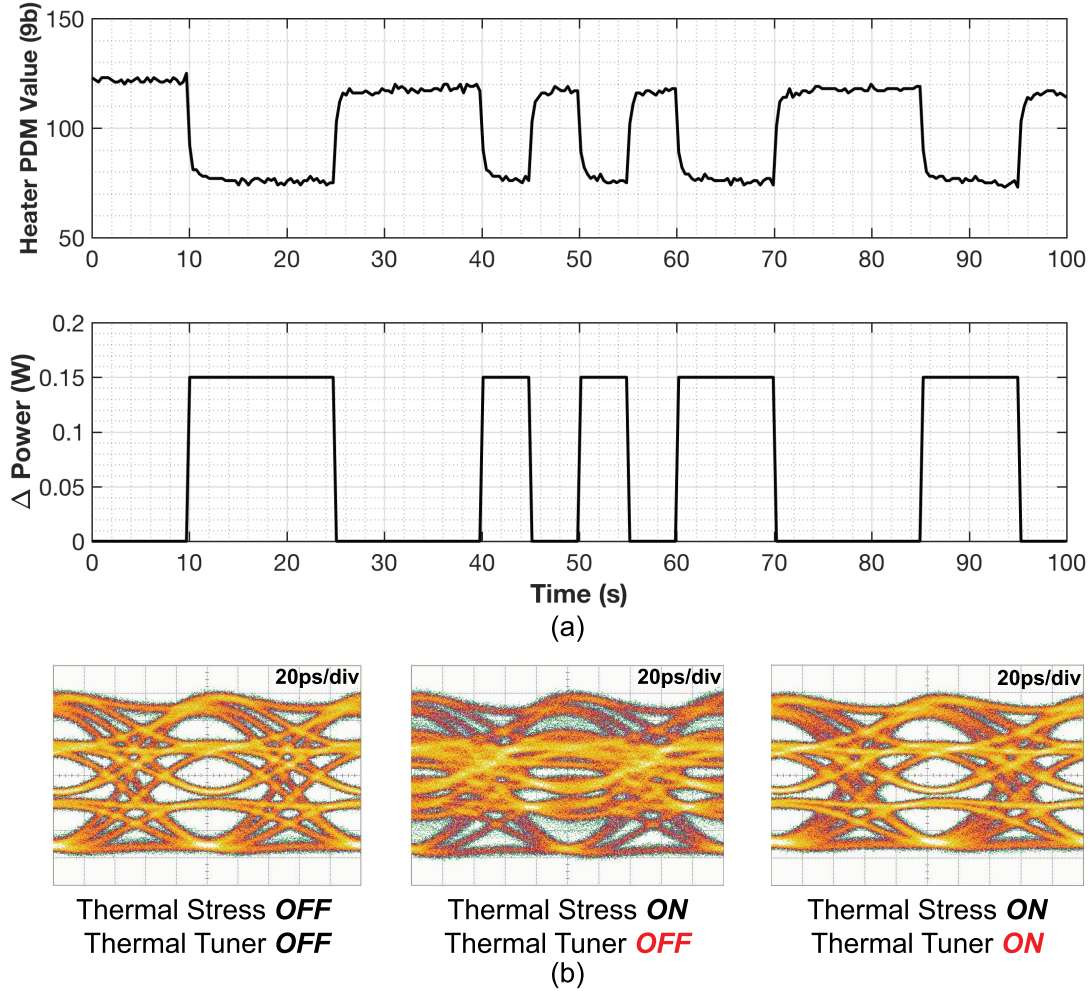


Fig. 18. (a) Thermal tuning stress test pattern and heater value during the active thermal tuning. (b) 20-Gb/s PAM-4 transmit eye diagrams with thermal tuning ON and OFF.

improve the drivers' voltage swing up to 2.4 V in this process. Data path is designed using CMOS digital standard cells. This makes the design easily portable to advanced nodes without the need of designing a high-speed electrical DAC. The ODAC is operating in the depletion mode with a swing of 0 to  $-1.55$  V.

## VII. EXPERIMENTAL DEMONSTRATION

The transmitter is designed and fabricated in a multi-project wafer run in the 45-nm SOI CMOS technology along with other electrical designs. Assuming a dedicated DPLL, the transmitter occupies the area of  $0.06 \text{ mm}^2$  including clocking blocks (Fig. 13). The die is flip-chip assembled onto a PCB and undergone substrate removal afterward (Fig. 14). A tunable laser source is coupled into the backside of the chip via a lensed fiber and unidirectional vertical couplers on the chip with 3-dB loss at 1280-nm wavelength and the modulated light is directly fed in to a 30-GHz optical scope without any optical amplification. Fig. 15(a) presents the ODAC's static characteristics for codes used for the PAM-4 transmission measurement. The microring modulator achieved a free spectral range of 3.2-THz and Q-factor of 6.5 k.

This microring design is over-coupled since the bus waveguide/ring gap was originally designed for the 1180-nm wavelength. This measurement also confirms that the  $R_{LM}$  of about 98% is achievable at the maximum OMA<sub>TX</sub> wavelength without any pre-distortion. ODAC's transmission is also indirectly measured for all 16 codes by running the transmitter in pattern mode with four different code settings to measure all possible transmissions at the output [Fig. 15(b)].

The measured 10%-90% rise/fall time is 20-ps indicating that transmitter can potentially run faster than 20 GS/s. The transmitted eye diagram (captured via a 30-GHz optical scope module) is open with 3-dB ER and 5.5-dB IL at 1285-nm laser wavelength (Fig. 16). ER and IL can be improved by critically coupling the ring. In addition, using higher swing drivers can further enhance the performance as the junctions are not yet fully depleted. Optimal numbers of depleted segments corresponding to PAM-4 symbols are (0, 5, 10, 15) to achieve balanced PAM-4 transmit eye diagram without any pre-distortion. The modulator and drivers achieved 20-Gb/s data rate in the NRZ mode with 155-fJ/b and 40-Gb/s PAM-4 with 42-fJ/b energy efficiency. Higher energy consumption per symbol for NRZ was expected due to the higher transition

TABLE I  
SUMMARY AND COMPARISON WITH PRIOR HIGH-SPEED OPTICAL TRANSMITTERS

	This Work	[20]	[11]	[16]	[8]
<b>Technology</b>					
Photonics Circuits	45 nm CMOS SOI	130 nm SOI GP 65 nm CMOS	90 nm CMOS SOI	130 nm SOI CMOS 40 nm CMOS	PIC25G SOI 55 nm BiCMOS
Integration	Monolithic	Wirebond	Monolithic	Wirebond	Cu-Pt 3D (copper pillars)
Wavelength	1280 nm	1550 nm	1300 nm	1310 nm	1310 nm
<b>Transmitter</b>					
Driver Supply	1.55 V	2.4 V	1.5 V	1 V	N/R
Modulator Device	Ring-resonator	Ring-resonator	MZI	SISCAP-MZI ¶	MZI
Extinction	3 dB	7 dB	6.3 dB	N/R	2.5 dB
Insertion Loss	5.5 dB	5 dB	5 dB	N/R	>5.7 dB†
NRZ Data Rate	20 Gb/s	N/A	25 Gb/s	20 Gb/s	56 Gb/s
NRZ Energy Efficiency*	0.155 pJ/bit	N/A	N/R	4.5 pJ/bit	5.4 pJ/bit
PAM-4 Data Rate	40 Gb/s	40 Gb/s	56 Gb/s	20 Gb/s	N/A
PAM-4 Energy Efficiency*	0.042 pJ/bit	3.04 pJ/bit	4.8 pJ/bit	0.29 pJ/bit	N/A
Photonics Area	0.01 mm <sup>2</sup>	0.01 mm <sup>2</sup> †	1.5 mm <sup>2</sup> †	0.18 mm <sup>2</sup>	2.3 mm <sup>2</sup> †
Driver Area	0.001 mm <sup>2</sup> ‡	0.07 mm <sup>2</sup> †	1.5 mm <sup>2</sup> †	0.18 mm <sup>2</sup> †	0.45 mm <sup>2</sup> †
Modulator and Driver BW Density	3.6 Tb/s/mm <sup>2</sup>	0.5 Tb/s/mm <sup>2</sup>	0.036 Tb/s/mm <sup>2</sup>	0.053 Tb/s/mm <sup>2</sup>	0.02 Tb/s/mm <sup>2</sup>
Total Transmitter Area	0.06 mm <sup>2</sup> §	0.08 mm <sup>2</sup>	1.56 mm <sup>2</sup>	0.38 mm <sup>2</sup>	2.75 mm <sup>2</sup>

N/A = Not Applicable, N/R = Not Reported  
\* Modulator and Driver Energy Efficiency  
† Estimated from figures  
‡ Including LUT  
¶ Silicon-insulator-silicon Capacitor MZI

probabilities and different wiring capacitance of segments. The energy efficiency of the complete transmitter at 40 Gb/s PAM-4 is 685-fJ/b. Area/energy breakdown is summarized in Fig. 17. Area and energy are dictated by the clocking, which can be amortized by sharing the DPLL among multiple transmitters due to a small transmitter form factor that simplifies the clock distribution. Thermal tuning functionality is verified up to 20-Gb/s PAM-4 transmission due to a timing violation issue in the digital controller for higher data rates. In this stress test, after the tuner locked the ring into the maximum eye-opening point by tracking “3”-level symbol, we turned ON and OFF the other test sites around this transmitter on the die to create “hot spots” with a fixed random pattern [Fig. 18(a)]. Transmit eye diagrams for a fixed bit-stream are captured via an ac-coupled external TIA with 10-GHz bandwidth. The eye is completely closed without the thermal tuning while active thermal tuning kept the PAM-4 eyes open by adjusting the heater strength according to the injected ambient heat [Fig. 18(b)].

### VIII. COMPARISON

The performance of our PAM-4 transmitter is summarized in Table I and compared against other high-speed optical transmitters. This paper proves the benefits of eliminating the electrical DAC and using microrings and the advantages of monolithic silicon photonics platforms to achieve energy efficiency. These elements improved both total energy efficiency (685-fJ/b) and bandwidth density (0.67 Tb/s/mm<sup>2</sup>) over the state-of-the-art MZI and microring-based transmitters.

### IX. CONCLUSION

We have demonstrated a DWDM compatible PAM-4 transmitter based on a digital-to-optical converter design using

segmented microring resonators in a commercial 45-nm SOI CMOS process. This device can be used to support even higher order modulations such as PAM-8/16 as well as the high-speed and moderate-resolution (5–7 bits) optical AWGs. In addition to high energy efficiency, the complete transmitter occupies only 0.06 mm<sup>2</sup> achieving bandwidth density of 0.67 Tb/s/mm<sup>2</sup> including the PLL, which makes this approach suitable for systems-on-chip such as processors and switches with a large number of I/O links.

### ACKNOWLEDGMENT

The authors would like to thank T. Kim, N. Mehta, P. Bhargava, and the Berkeley Wireless Research Center staff. The views expressed are those of the authors and do not reflect the official policy or position of the DoD or the U.S. Government.

### REFERENCES

- [1] Y. A. Vlasov, “Silicon CMOS-integrated nano-photonics for computer and data communications beyond 100 G,” *IEEE Commun. Mag.*, vol. 50, no. 2, pp. s67–s72, Feb. 2012.
- [2] C. Kachris and I. Tomkos, “A survey on optical interconnects for data centers,” *IEEE Commun. Surveys Tuts.*, vol. 14, no. 4, pp. 1021–1036, 4th Quart., 2012.
- [3] D. Vantrease *et al.*, “Corona: System implications of emerging nanophotonic technology,” in *Proc. 35th Int. Symp. Comput. Archit. (ISCA)*, Jun. 2008, pp. 153–164.
- [4] S. Beamer *et al.*, “Re-architecting DRAM memory systems with monolithically integrated silicon photonics,” in *Proc. 37th Annu. Int. Symp. Comput. Archit.*, 2010, pp. 129–140.
- [5] M. Rakowski *et al.*, “A 4×20 Gb/s WDM ring-based hybrid CMOS silicon photonics transceiver,” in *IEEE Int. Solid-State Circuits Conf. (ISSCC) Dig. Tech. Papers*, Feb. 2015, pp. 1–3.
- [6] K. T. Settaluri *et al.*, “Demonstration of an optical chip-to-chip link in a 3D integrated electronic-photonic platform,” in *Proc. 41st Eur. Solid-State Circuits Conf. (ESSCIRC)*, Sep. 2015, pp. 156–159.

- [7] E. Timurdogan *et al.*, "An ultra low power 3D integrated intra-chip silicon electronic-photonic link," in *Proc. Opt. Fiber Commun. Conf. (OFC)*, Mar. 2015, pp. 1–3.
- [8] E. Temporiti, G. Minoia, M. Repossi, D. Baldi, A. Ghilioni, and F. Svelto, "A 56 Gb/s 300 mW silicon-photonics transmitter in 3D-integrated PIC25G and 55 nm BiCMOS technologies," in *IEEE Int. Solid-State Circuits Conf. (ISSCC) Dig. Tech. Papers*, Jan. 2016, pp. 404–405.
- [9] C. Sun *et al.*, "Single-chip microprocessor that communicates directly using light," *Nature*, vol. 528, no. 7583, pp. 534–538, 2015.
- [10] J. F. Buckwalter, X. Zheng, G. Li, K. Raj, and A. V. Krishnamoorthy, "A monolithic 25-Gb/s transceiver with photonic ring modulators and Ge detectors in a 130-nm CMOS SOI process," *IEEE J. Solid-State Circuits*, vol. 47, no. 6, pp. 1309–1322, Jun. 2012.
- [11] C. Xiong, D. M. Gill, J. E. Proesel, J. S. Orcutt, W. Haensch, and W. M. J. Green, "Monolithic 56 Gb/s silicon photonic pulse-amplitude modulation transmitter," *Optica*, vol. 3, no. 10, pp. 1060–1065, Oct. 2016.
- [12] C. Sun *et al.*, "A monolithically-integrated chip-to-chip optical link in bulk CMOS," *IEEE J. Solid-State Circuits*, vol. 50, no. 4, pp. 828–844, Apr. 2015.
- [13] X. Zheng *et al.*, "Efficient WDM laser sources towards terabyte/s silicon photonic interconnects," *J. Lightw. Technol.*, vol. 31, no. 24, pp. 4142–4154, Dec. 15, 2013.
- [14] B. R. Koch *et al.*, "Integrated silicon photonic laser sources for telecom and datacom," in *Proc. Opt. Fiber Commun. Conf. (OFC)*, Mar. 2013, pp. 1–3.
- [15] M. R. Watts, W. A. Zortman, D. C. Trotter, R. W. Young, and A. L. Lentine, "Low-voltage, compact, depletion-mode, silicon Mach-Zehnder modulator," *IEEE J. Sel. Topics Quantum Electron.*, vol. 16, no. 1, pp. 159–164, Jan. 2010.
- [16] X. Wu *et al.*, "A 20 Gb/s NRZ/PAM-4 1 V transmitter in 40 nm CMOS driving a Si-photonic modulator in 0.13  $\mu\text{m}$  CMOS," in *IEEE Int. Solid-State Circuits Conf. (ISSCC) Dig. Tech. Papers*, Feb. 2013, pp. 128–129.
- [17] M. Pantouvaki, P. Verheyen, J. D. Coster, G. Lepage, P. Absil, and J. V. Campenhout, "56 Gb/s ring modulator on a 300 nm silicon photonics platform," in *Proc. Eur. Conf. Opt. Commun. (ECOC)*, Sep. 2015, pp. 1–3.
- [18] C. Sun *et al.*, "A 45 nm CMOS-SOI monolithic photonics platform with bit-statistics-based resonant microring thermal tuning," *IEEE J. Solid-State Circuits*, vol. 51, no. 4, pp. 893–907, Apr. 2016.
- [19] I. L. Gheorma and R. M. Osgood, "Fundamental limitations of optical resonator based high-speed EO modulators," *IEEE Photon. Technol. Lett.*, vol. 14, no. 6, pp. 795–797, Jun. 2002.
- [20] A. Roshan-Zamir *et al.*, "A 40 Gb/s PAM4 silicon microring resonator modulator transmitter in 65 nm CMOS," in *Proc. IEEE Opt. Interconnects Conf. (OI)*, May 2016, pp. 8–9.
- [21] J. S. Orcutt *et al.*, "Open foundry platform for high-performance electronic-photonic integration," *Opt. Exp.*, vol. 20, no. 11, pp. 12222–12232, May 2012.
- [22] T. Yilmaz, C. M. DePriest, T. Turpin, J. H. Abeles, and P. J. Delfyett, "Toward a photonic arbitrary waveform generator using a modelocked external cavity semiconductor laser," *IEEE Photon. Technol. Lett.*, vol. 14, no. 11, pp. 1608–1610, Nov. 2002.
- [23] M. H. Khan *et al.*, "Ultrabroad-bandwidth arbitrary radiofrequency waveform generation with a silicon photonic chip-based spectral shaper," *Nature Photon.*, vol. 4, no. 2, pp. 117–122, Feb. 2010.
- [24] J. Wang *et al.*, "Reconfigurable radio-frequency arbitrary waveforms synthesized in a silicon photonic chip," *Nature Commun.*, vol. 6, p. 5957, Jan. 2015.
- [25] R. Soref and B. Bennett, "Electro-optical effects in silicon," *IEEE J. Quantum Electron.*, vol. QE-23, no. 1, pp. 123–129, Jan. 1987.
- [26] Q. Xu, B. Shmidt, S. Pradhan, and M. Lipson, "Micrometre-scale silicon electro-optic modulator," *Nature*, vol. 435, no. 7040, pp. 325–327, May 2005.
- [27] H. Li *et al.*, "A 25 Gb/s, 4.4 V-swing, AC-coupled ring modulator-based WDM transmitter with wavelength stabilization in 65 nm CMOS," *IEEE J. Solid-State Circuits*, vol. 50, no. 12, pp. 3145–3159, Dec. 2015.
- [28] M. T. Wade *et al.*, "Energy-efficient active photonics in a zero-change, state-of-the-art CMOS process," in *Proc. Opt. Fiber Commun. Conf. (OFC)*, Mar. 2014, pp. 1–3.
- [29] A. Cebrero *et al.*, "A 64 Gb/s 1.4 pJ/b NRZ optical-receiver data-path in 14 nm CMOS FinFET," in *IEEE Int. Solid-State Circuits Conf. (ISSCC) Dig. Tech. Papers*, Feb. 2017, pp. 482–483.
- [30] M. H. Nazari and A. Emami-Neyestanak, "A 24-Gb/s double-sampling receiver for ultra-low-power optical communication," *IEEE J. Solid-State Circuits*, vol. 48, no. 2, pp. 344–357, Feb. 2013.
- [31] E. Sackinger, "The transimpedance limit," *IEEE Trans. Circuits Syst. I, Reg. Papers*, vol. 57, no. 8, pp. 1848–1856, Aug. 2010.
- [32] B. Wang, K. Yu, H. Li, P. Y. Chiang, and S. Palermo, "Energy efficiency comparisons of NRZ and PAM4 modulation for ring-resonator-based silicon photonic links," in *Proc. IEEE 58th Int. Midwest Symp. Circuits Syst. (MWSCAS)*, Aug. 2015, pp. 1–4.
- [33] K. T. Settaluri, C. Lalau-Keraly, E. Yablonovitch, and V. Stojanović, "First principles optimization of opto-electronic communication links," *IEEE Trans. Circuits Syst. I, Reg. Papers*, vol. 64, no. 5, pp. 1270–1283, May 2017.
- [34] S. Narasimha *et al.*, "High performance 45-nm SOI technology with enhanced strain, porous low- $k$  BEOL, and immersion lithography," in *IEDM Tech. Dig.*, Dec. 2006, pp. 1–4.
- [35] M. T. Wade *et al.*, "75% efficient wide bandwidth grating couplers in a 45 nm microelectronics CMOS process," in *Proc. IEEE Opt. Interconnects Conf. (OI)*, Apr. 2015, pp. 46–47.
- [36] J. Notaros *et al.*, "Ultra-efficient CMOS fiber-to-chip grating couplers," in *Proc. Opt. Fiber Commun. Conf. (OFC)*, Mar. 2016, pp. 1–3.
- [37] L. Alloatti and R. J. Ram, (Jan. 2016). "Resonance-enhanced waveguide-coupled silicon-germanium detector." [Online]. Available: <https://arxiv.org/abs/1601.00542>
- [38] A. H. Atabaki, H. Meng, L. Alloatti, and R. J. Ram, "A high-speed photodetector for telecom, Ethernet, and FTTH applications in zero-change CMOS process," in *Proc. Opt. Fiber Commun. Conf. (OFC)*, Mar. 2016, pp. 1–3.
- [39] J. M. Shainline *et al.*, "Depletion-mode carrier-plasma optical modulator in zero-change advanced CMOS," *Opt. Lett.*, vol. 38, no. 15, pp. 2657–2659, 2013.
- [40] L. Alloatti, D. Cheian, and R. J. Ram, "High-speed modulator with interleaved junctions in zero-change CMOS photonics," *Appl. Phys. Lett.*, vol. 108, no. 13, p. 131101, 2016.
- [41] J. Crossley, E. Naviasky, and E. Alon, "An energy-efficient ring-oscillator digital PLL," in *Proc. IEEE Custom Integr. Circuits Conf. (CICC)*, Sep. 2010, pp. 1–4.
- [42] S. K. Selvaraja, W. Bogaerts, P. Dumon, D. V. Thourhout, and R. Baets, "Subnanometer linewidth uniformity in silicon nanophotonic waveguide devices using CMOS fabrication technology," *IEEE J. Sel. Topics Quantum Electron.*, vol. 16, no. 1, pp. 316–324, Jan. 2010.
- [43] J. S. Orcutt *et al.*, "Nanophotonic integration in state-of-the-art CMOS foundries," *Opt. Exp.*, vol. 19, no. 3, pp. 2335–2346, Jan. 2011.



**Sajjad Moazeni** (S'14) received the B.S. degree in electrical engineering from the Sharif University of Technology, Tehran, Iran, in 2013, and the M.S. degree in electrical engineering from the University of California, Berkeley, CA, USA, in 2016, where he is currently pursuing the Ph.D. degree in electrical engineering and computer science.

He was with the Mixed-Signal Design Group, Oracle America, Inc., in 2015. He is now member of the Berkeley Wireless Research Center, University of California, Berkeley. His current research interests include integrated and silicon photonics, energy-efficient electro-optical devices and systems, bio photonics, and analog/mixed-signal integrated circuits.



**Sen Lin** received the B.S. degree in microelectronics from Tsinghua University, Beijing, China, in 2012. He is currently pursuing the Ph.D. degree with Prof. Vladimir Stojanović's Group, University of California at Berkeley, Berkeley, CA, USA.

He is a member of the Berkeley Wireless Research Center, University of California at Berkeley. He has also been with Xilinx, Inc., San Jose, CA, USA, as an Analog/Mixed-Signal Design Intern since 2015. His current research interests include design and modeling of silicon photonic systems and high-speed communication links.



**Mark Wade** received the B.S. degrees in electrical engineering and physics from Louisiana Tech University, Ruston, LA, USA, in 2010, and the M.S. and Ph.D. degrees in electrical engineering from the University of Colorado, Boulder, CO, USA, in 2013 and 2015, respectively, where he focused on integrated photonic devices for electronic-photonics wavelength division multiplexed communication systems.

Dr. Wade was a NIST Measurement, Science, and Engineering Fellow and a National Science Foundation Graduate Research Fellow. In 2015, he co-founded Ayar Labs.



**Luca Alloatti** received the M.Sc. degree in physics from the University of Pisa, Pisa, Italy, in 2004, the “Diploma di Licenza” from the Scuola Normale Superiore di Pisa, Pisa, in 2006, and the Ph.D. degree in electrical engineering from the Karlsruhe Institute of Technology, Karlsruhe, Germany, in 2012, with a thesis entitled “High-Speed, Low-Power, and Mid-IR Silicon Photonics Applications.”

He joined the Massachusetts Institute of Technology, Cambridge, MA, USA, in 2013, where he demonstrated “zero-change CMOS” high-speed detectors and modulators as well as a photonic design automation infrastructure based on Cadence. Since 2015, he has been a Research Scientist at ETH-Zurich, Zurich, Switzerland.



**Rajeev J. Ram** (F’16) received the B.S. degree in applied physics from the California Institute of Technology, Pasadena, CA, USA, in 1991, and the Ph.D. degree in electrical engineering from the University of California, Santa Barbara, CA, USA, in 1997.

He is currently a Professor with the Massachusetts Institute of Technology, Cambridge, MA, USA. His current research interests include physical optics and electronics, including the development of novel components and systems for communications and sensing and studies of fundamental interactions between electronic materials and light.

Dr. Ram is a Fellow of OSA.



**Miloš Popović** (M’05) was born in Zaječar, Serbia, in 1977. He received the B.Sc.E. degree in electrical engineering from Queen’s University, Kingston, ON, Canada, in 1999, and the M.S. and Ph.D. degrees in electrical engineering from the Massachusetts Institute of Technology, Cambridge, MA, USA, in 2002 and 2008, respectively.

From 2010 to 2016, he was an Assistant Professor of electrical engineering with the University of Colorado Boulder, Boulder, CO, USA. Since 2016, he has been with the Department of Electrical and Computer Engineering, Boston University, Boston, MA, USA. He is the inventor or co-inventor of over 18 patents, and has authored or co-authored over 165 research papers and two book chapters. His current research interests include silicon photonic circuits, CMOS photonics integration and optical interconnects, nonlinear and quantum integrated photonics, and light-forces-based nanomechanical photonic devices, and also include electromagnetic theory and numerical methods related to photonics. Dr. Popović has served on technical program committees for various OSA and IEEE conferences. In 2012, he was named a Fellow of the David & Lucile Packard Foundation.



**Vladimir Stojanović** (SM’16) received the Dipl.Ing. degree from the University of Belgrade, Belgrade, Serbia, in 1998, and the Ph.D. degree in electrical engineering from Stanford University, Stanford, CA, USA, in 2005.

He was with Rambus, Inc., Los Altos, CA, USA, as a Principal Engineer from 2001 to 2004, and with the Massachusetts Institute of Technology, Cambridge, MA, USA, as an Associate Professor from 2005 to 2013. He is an Associate Professor of electrical engineering and computer sciences with the University of California, Berkeley, CA, USA. His current research interests include design, modeling, and optimization of integrated systems from CMOS-based VLSI blocks and interfaces to system design with emerging devices like NEM relays and silicon photonics, and also include the design and implementation of energy-efficient electrical and optical networks, and digital communication techniques in high-speed interfaces and high-speed mixed-signal IC design.

Dr. Stojanović was a recipient of the 2006 IBM Faculty Partnership Award, the 2009 NSF CAREER Award, the 2008 ICCAD William J. McCalla, the 2008 IEEE TRANSACTIONS ON ADVANCED PACKAGING, and the 2010 ISSCC Jack Raper Best Paper Awards. He was an IEEE Solid-State Circuits Society Distinguished Lecturer from 2012 to 2013.